Article

Facile In Situ Synthesis of Co(OH)$_2$–Ni$_3$S$_2$ Nanowires on Ni Foam for Use in High-Energy-Density Supercapacitors

Xuan Liang Wang [1,†], En Mei Jin [1,†], Jiasheng Chen [1], Parthasarathi Bandyopadhyay [1], Bo Jin [2] and Sang Mun Jeong [1,*]

1 Department of Chemical Engineering, Chungbuk National University, 1 Chungdae-ro, Seowon-gu, Cheongju 28644, Chungbuk, Korea; wangxuanleon@gmail.com (X.L.W.); jinenmei@chungbuk.ac.kr (E.M.J.); chenjs3824@gmail.com (J.C.); partha012@gmail.com (P.B.)
2 Key Laboratory of Automobile Materials, Ministry of Education, and College of Materials Science and Engineering, Jilin University, Changchun 130022, China; jinbo@jlu.edu.cn
* Correspondence: smjeong@chungbuk.ac.kr
† These authors contributed equally to this work.

Abstract: Ni$_3$S$_2$ nanowires were synthesized in situ using a one-pot hydrothermal reaction on Ni foam (NF) for use in supercapacitors as a positive electrode, and various contents (0.3−0.6 mmol) of Co(OH)$_2$ shells were coated onto the surfaces of the Ni$_3$S$_2$ nanowire cores to improve the electrochemical properties. The Ni$_3$S$_2$ nanowires were uniformly formed on the smooth NF surface, and the Co(OH)$_2$ shell was formed on the Ni$_3$S$_2$ nanowire surface. By direct NF participation as a reactant without adding any other Ni source, Ni$_3$S$_2$ was formed more closely to the NF surface, and the Co(OH)$_2$ shell suppressed the loss of active material during charging–discharging, yielding excellent electrochemical properties. The Co(OH)$_2$–Ni$_3$S$_2$/Ni electrode produced using 0.5 mmol Co(OH)$_2$ (Co$_{0.5}$–Ni$_3$S$_2$/Ni) exhibited a high specific capacitance of 1837 F g^{-1} (16.07 F cm^{-2}) at a current density of 5 mA cm^{-2}, and maintained a capacitance of 583 F g^{-1} (16.07 F cm^{-2}) at a much higher current density of 50 mA cm^{-2}. An asymmetric supercapacitor (ASC) with Co(OH)$_2$–Ni$_3$S$_2$ and active carbon displayed a high-power density of 1036 kW kg^{-1} at an energy density of 43 W h kg^{-1} with good cycling stability, indicating its suitability for use in energy storage applications. Thus, the newly developed core–shell structure, Co(OH)$_2$–Ni$_3$S$_2$, was shown to be efficient at improving the electrochemical performance.

Keywords: nickel sulfide; cobalt hydroxides; core–shell; high energy density; asymmetric supercapacitor

1. Introduction

Currently, the main concerns in society are efficient energy storage and clean energy. Supercapacitors are the most ideal devices for use in clean energy storage, owing to their low costs, rapid discharge rates, and high electrochemical activities, in addition to mechanical and thermal stabilities [1,2]. However, despite numerous advantages, supercapacitors exhibit lower energy densities (~10 W h kg^{-1}) compared to those of Li-ion batteries (LIBs, typically <300 Wh kg^{-1}) [3,4]. Supercapacitors can be divided into electrochemical double-layer capacitors (EDLCs) and pseudocapacitors. EDLCs employ an electric double layer formed at the interface of an electrolyte and a polarizable electrode, such as activated carbon (AC), and pseudocapacitors are based on the Faradaic electrochemical redox mechanism of charge storage [5]. Carbons with high surface areas are mainly used in EDLCs, whereas in pseudocapacitor research, oxides, such as ruthenium and manganese, are mainly used. According to a review of recent advances in carbon–based materials for use in supercapacitor electrodes, the specific energy is generally <10 Wh kg^{-1} [3,6,7]. Recently, mono– and bimetallic oxides, layered double hydroxides, and transition metal sulfides were proposed to overcome the lower energy densities in supercapacitors [8–11]. The transition metal sulfides (nickel or cobalt sulfide) exhibited considerable potential; in particular, nickel

sulfides exhibit excellent electrochemical energy storage and fascinating properties, such as excellent redox reversibility, conductivities, and capacitances [12–15]. However, low-rate capability and poor electrochemical stability limit practical applications because of the surface Faradaic redox reactions and reverse kinetics during rapid charge−discharge [16]. Nickel sulfides have various phases, such as α– and β–NiS, NiS_2, and Ni_3S_2 are low−cost, abundant materials with widespread applications, such as LIB and supercapacitor electrode materials [17–20].

The most recently reported nickel sulfide-based research mainly focuses on engineering vacancies including control of morphologies and phase crystallinities, binding them with other carbon materials, and doping to optimize electrochemical performance [21–25]. For example, Chou et al. prepared a binder-free flaky Ni_3S_2 electrode as a positive material that displayed a high specific capacitance (SC) of 717 F g^{-1} at 2 A g^{-1} and excellent cycle retention of 91% [24]. Krishnamoorthy et al. used a one-pot hydrothermal method to prepare nest–type Ni_3S_2 with an SC of 1293 F g^{-1} at 5 mA cm^{-2} [25]. Li et al. used single–crystal β–NiS nanorod arrays to synthesize Ni_3S_2@β−NiS materials with novel 3D architectures and pine twig-like morphologies in hollow Ni_3S_2 porous frameworks, with an SC of 1158 F g^{-1} at 2 A g^{-1} [26]. Hu et al. proposed a phase modulation strategy dominated by a novel coordination agent supported by a hydrothermal process [27].

In addition, the crystallization and morphology of nickel sulfide are primarily tuned by controlling the sulfur source in the reaction. In general, nickel sulfide is synthesized by dissolving metal salts, such as nickel acetate, nitrate, and chloride, and sulfur precursors, such as sodium sulfate, thioacetamide (TAA), thiourea (TU), and sodium thiosulfate, in solution [28–34]. Chen et al. used $Ni(NO_3)_2 \cdot 6H_2O$ and TU to directly prepare Ni_3S_2 on Ni foam (NF) [35], and Wu et al. used TAA and NF to prepare rod–like Ni_3S_2 [36].

In addition, numerous studies were conducted to evaluate core–shell structures to improve the electrochemical properties of Ni_3S_2-based supercapacitors [37–40]. The core–shell structure protects the active material, ensuring excellent cycle stability during charging and discharging. However, multi-step reactions are generally performed to prepare core–shell structures. For example, Chen et al. used a two-step hydrothermal reaction to fabricate the core–shell structures of Ni_3S_2@$Co(OH)_2$ nanowires formed directly on NF for use in asymmetric supercapacitors (ASCs), and the Ni_3S_2@$Co(OH)_2$ electrode exhibiting a high SC of 2139.4 F g^{-1} at 2 mA cm^{-2}, and maintaining a capacitance of 1139.4 F g^{-1} at 40 mA cm^{-2} [37].

In this study, the core–shell structured $Co(OH)_2−Ni_3S_2$ was synthesized in situ using a one–step hydrothermal reaction on NF as a binder-free positive electrode for use in supercapacitors. By direct NF participation as a reactant, without adding any other Ni source, Ni_3S_2 was formed more closely to the NF surface, and the $Co(OH)_2$ shell suppressed the loss of active material during charging–discharging. Moreover, NF provides sufficient microcavities for simple penetration of electrolyte ions and rapid transport of the generated gas. To suppress the active material loss during cycling, various amounts of Co were added to control the thickness of the shell, yielding excellent electrochemical properties. In addition, the electrochemical properties were investigated by assembling an ASC using $Co(OH)_2−Ni_3S_2$ and AC as the positive electrode and negative electrode, respectively.

2. Experimental
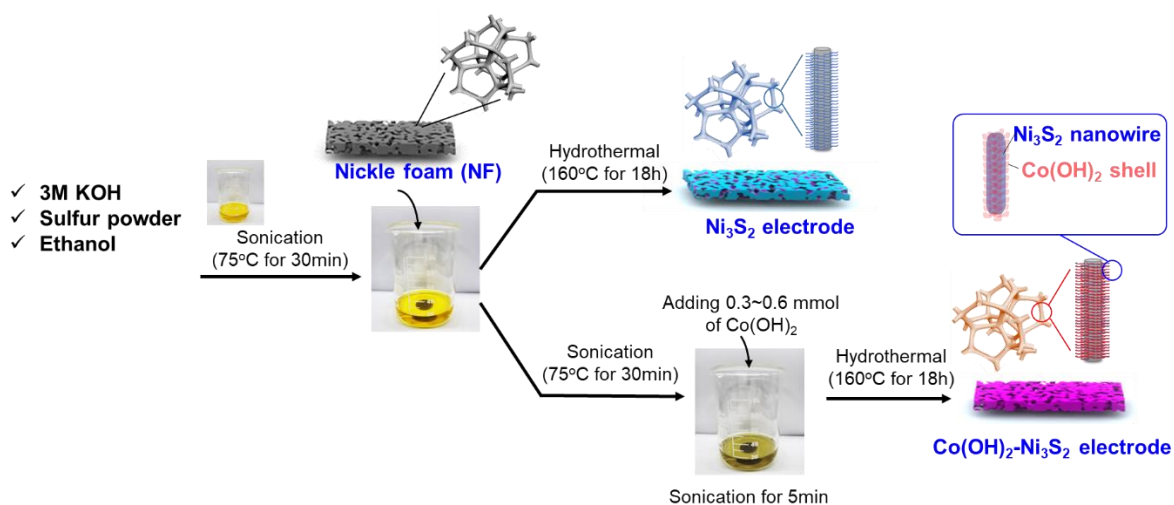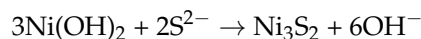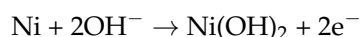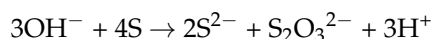
2.1. Materials

KOH (95%), sulfur powder, and $CoCl_2 \cdot 6H_2O$ (98%) were obtained from Sigma–Aldrich (St. Louis, MO, USA). For ethyl alcohol (anhydrous, 99%), SAMCHUN chemicals (Gyeonggi-do, Republic of Korea) products were used, and for nickel form (NF, 99.5%), Goodfellow (Huntingdon, UK) products with a thickness of 1.5 mm and a bulk density of 0.45 g/cm^3 were used.

2.2. Synthesis of Ni₃S₂ and Co(OH)₂–Ni₃S₂ Positive Electrode

Ni_3S_2 nanowires for use as positive active materials were synthesized using a one-pot hydrothermal reaction. For synthesizing the Ni_3S_2 nanowires, the NF (2×1 cm^2) was used as the reactant and substrate. First, NF was sonicated in 3 M HCl for 30 min, and then washed for 30 min by deionized water and ethanol with volume ration of 1:1 to remove organic impurities and surface oxidized layer. The washed NF was subsequently vacuum-dried overnight at 50 °C.

The detailed experimental procedure for synthesizing the NF–supported Ni_3S_2 nanowires is shown in Figure 1. The source of sulfur was the natural sulfur powder in molar ratios of 2 mmol. Sulfur powder (99.5%) was added to 8 mL of 3 M KOH and sonicated at 70 °C until the solution turned transparent yellow. A total of 8 mL of ethyl alcohol and NF (2×1 cm^2) were then added, and the solution was sonicated for a few minutes. Subsequently, the uniform solution was transferred to hydrothermal reactor. The reactor was heated for 18 h at 160 °C. The product, Ni_3S_2, was collected after the reaction system was cooled to below 30 °C. Thereafter, the Ni_3S_2 film was washed and vacuum–dried at 50 °C overnight. During the hydrothermal process, sulfur reacts with the NF to uniformly deposit Ni_3S_2 on the NF surface. The reaction formula for the formation of nickel sulfide on the NF may be as below:

$$3OH^- + 4S \rightarrow 2S^{2-} + S_2O_3^{2-} + 3H^+$$

$$Ni + 2OH^- \rightarrow Ni(OH)_2 + 2e^-$$

$$3Ni(OH)_2 + 2S^{2-} \rightarrow Ni_3S_2 + 6OH^-$$

Figure 1. Schematic diagram of hydrothermal Ni_3S_2 and $Co(OH)_2$–Ni_3S_2 production.

For preparation of core–shell structured $Co(OH)_2$–Ni_3S_2, after all sonication steps were completed, the 0.3, 0.4, 0.5, or 0.6 mmol of the source of cobalt was added and in the solution, followed by hydrothermal reaction at 160 °C for 18 h. The 0.3, 0.4, 0.5, or 0.6 mmol cobalt–containing $Co(OH)_2$–Ni_3S_2 electrodes are denoted as $Co_{0.3}$–, $Co_{0.4}$–, $Co_{0.5}$–, and $Co_{0.6}$–Ni_3S_2, with a mass loading of 6.2, 6.8, 7.3, and 8.1 mg cm^{-2}, respectively.

2.3. Cell Assembly

For the electrochemical performance study, a three-electrode system was assembled using material formed in situ on NF (area $\approx 1 \times 1$ cm^2). Ni_3S_2 or $Co(OH)_2$–Ni_3S_2 was used as the working electrode and Ag/AgCl and a Pt plate were used as the reference and counter electrodes, respectively. In the three-electrode configuration, 3 M KOH solution was used as the electrolyte.

The ASC device was assembled by $Co_{0.5}$–Ni_3S_2 and AC electrodes as the positive and as negative electrodes, respectively. KOH (3 M) and filter paper (Whatman 42) were used

as the electrolyte and separator, respectively. Prior to assembling the ASC device, the AC negative electrode was prepared as follows: super-p carbon black, polyvinylidene fluoride, and AC as the conductive material, binder, and active material, respectively, were mixed in a mass ratio of 1:1:8 in *N*–methyl–2–pyrrolidinone (NMP) to form a uniform slurry. The slurry was uniformly coated on a Ni mesh and dried in an electrical oven at 60 °C for 1 h. The dried electrode was pressed and vacuum–dried at 110 °C for a day. In addition, the filter paper and as–prepared $Co_{0.5}$–Ni_3S_2 were immersed in electrolyte for a day. The ASC device was then assembled by sequentially stacking the soaked $Co_{0.5}$–Ni_3S_2 electrode, filter paper, and AC electrode.

2.4. Materials Characterization and Electrochemical Measurements

The crystal structures and morphologies were characterized using X-ray diffraction (XRD, Ultima IV, Rigaku, Tokyo, Japan), field emission scanning electron microscopy (FE-SEM, LEO–1530, Carl Zeiss, Oberkochen, Germany), and FE transmission electron microscopy (FE–TEM, 200 KV, JEM–2100F, JEOL, Tokyo, Japan). To evaluate the elemental composition and oxidation state, X-ray photoelectron spectroscopy (XPS) was performed using a PHI Quantera–II (Ulvac–PHI, Chigasaki, Japan).

The electrochemical performance of the three-electrode configuration was measured using an Autolab electrochemical workstation (AUT84455, Metrohm, Herisau, Switzerland). Electrochemical impedance spectroscopy (EIS) was performed in the frequency range 10^5–10^{-2} Hz at an amplitude of 10 mV using an Autolab electrochemical workstation (PGSTAT302N, Metrohm, The Netherlands). All resistances were determined using the NOVA program (Version 1.10.4, Metrohm, The Netherlands) to fit the related EI spectra. Cyclic voltammetry (CV, WBCS3000L, WonATech, Seoul, Korea) was measured at a scanning rate of 0.1 mV s^{-1} in the voltage range 1.5–3.2 V, and charge–discharge studies were performed at 0.1 C with a cut-off voltage of 1.5–3.2 V.

### 3. Results and Discussion

The XRD patterns of the Ni_3S_2 and $Co(OH)_2$–Ni_3S_2 electrodes are shown in Figure 2. The XRD patterns of all samples are consistent with the hexagonal phase (JCPDS card no. 44–1418) in the R32(155) space group, with sharp, intense peaks at 2θ = 21.75°, 31.10°, 37.78°, 44.33°, 49.73°, 50.12°, 55.16°, and 55.34° representing the (101), (110), (003), (202), (113), (211), (122), and (300) diffraction planes, respectively [41]. Peaks representing the cubic phases corresponding to nickel (JCPDS card no. 87–0712) are observed at 2θ = 44.50° (111), 51.85° (200), and 76.38° (220) [42]. These nickel patterns are observed because Ni_3S_2 was formed on the NF. The $Co(OH)_2$–Ni_3S_2 electrodes exhibit hexagonal and cubic phases, and their patterns lack the characteristic peaks representing $Co(OH)_2$ because they overlap with the hexagonal peaks representing $Co(OH)_2$ and/or the amorphous phase, which is formed by the hydrothermal reaction after $CoCl_2$ addition [43]. Peaks representing $Co(OH)_2$ corresponding to the hexagonal phase (JCPDS card no. 45–0031) are typically observed at 2θ = 32.22° (100), 37.65° (101), 51.09° (102), and 57.63° (110) [44].

Figure 3 shows the surface morphologies of the Ni_3S_2 and $Co(OH)_2$–Ni_3S_2 electrodes with different Co contents were characterized using FE-SEM and elemental mapping analysis. Ni_3S_2 exhibits a smooth surface, with the Ni_3S_2 nanowires uniformly formed on the NF surface following the hydrothermal reaction, clearly indicating that the NF reacts with the added sulfur. The Ni_3S_2 nanowires form very uniformly in terms of length and thickness, and no other form of Ni_3S_2 is observed in the SEM images. As shown in the highly magnified SEM image of Ni_3S_2 (inset of Figure 3b), long, thin nanowires are observed, with an average diameter of ~150 ± 10 nm. As the amount of added Co increases, the smoothness of the nanowire surface decreases and the $Co(OH)_2$ shell thickness increases (Figure 3c–f), because $Co(OH)_2$ is only formed on the surfaces of the Ni_3S_2 nanowires, rendering their surfaces rough. A rough surface may exhibit high electrolyte adsorption capacity due to its large specific surface area, and $Co(OH)_2$ may suppress the Ni_3S_2 active material loss during the cycling, resulting in excellent electrochemical properties. In addition, as shown by the

side views of the elemental mapping images (Figure 3g,h), all elements are distributed uniformly on the nanowires. Therefore, the synthesis via hydrothermal reaction at 160 °C for 18 h is successful.
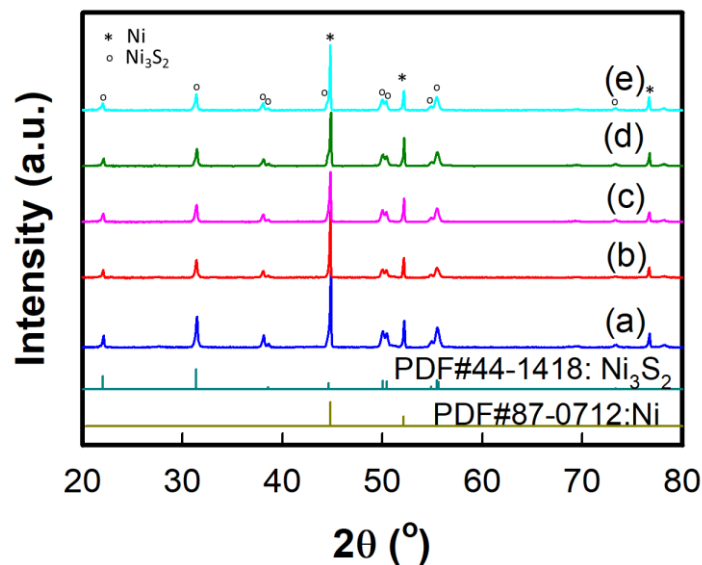

Figure 2. XRD patterns of the (**a**) N_3S_2, (**b**) $Co_{0.3}$–Ni_3S_2, (**c**) $Co_{0.4}$–Ni_3S_2, (**d**) $Co_{0.5}$–Ni_3S_2, and (**e**) $Co_{0.6}$–Ni_3S_2 electrodes.
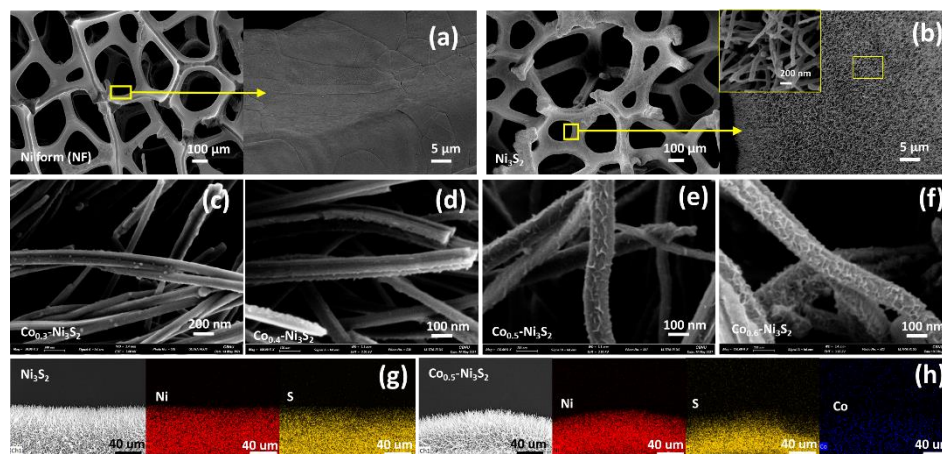
Figure 3. FE-SEM images at different magnifications and EDS mapping of (**a**) NF, (**b**) Ni_3S_2, (**c**) $Co_{0.3}$–Ni_3S_2, (**d**) $Co_{0.4}$–Ni_3S_2, (**e**) $Co_{0.6}$–Ni_3S_2, (**f**) $Co_{0.6}$–Ni_3S_2, (**g**) Ni_3S_2, and (**h**) $Co_{0.5}$–Ni_3S_2.

HRTEM was conducted to further explore the structures of the $Co_{0.5}$–Ni_3S_2 nanowires. As shown in Figure 4a,b, the Ni_3S_2 nanowires cores are uniformly covered by $Co(OH)_2$ nanosheets shells. The interphase between Ni_3S_2 and $Co(OH)_2$ is no clear boundary observed, indicating that a close contact was formed between them. Such a structure may result in improved electrochemical performance as it favors electron transfer during the Faradaic redox reactions [45]. The diameters of the core Ni_3S_2 nanowires are ~150 nm, and the $Co(OH)_2$ layers covering the Ni_3S_2 nanowires exhibit thicknesses in the range 20–40 nm. As shown in Figure 4c, the $Co_{0.5}$–Ni_3S_2 nanowires exhibit uniform distributions of Ni, S, and Co. This further confirming the formation of a uniform, well-defined core–shell structure. The HRTEM image of the $Co_{0.5}$–Ni_3S_2 nanowire (Figure 4d) reveals lattice spacings of 0.4, 0.28, and 0.24 nm, corresponding to the (110) and (101) interplanar spacings of Ni_3S_2 and the (101) interplanar spacings of $Co(OH)_2$, respectively. As shown in the selected area electron diffraction (SAED) pattern (Figure 4e), several distinct concentric

rings clearly indicate the polycrystallinity of Ni_3S_2, and the diffraction rings from inside to outside correspond to the (101), (110), (003), (202), (113), and (104) crystalline planes of Ni_3S_2, respectively.
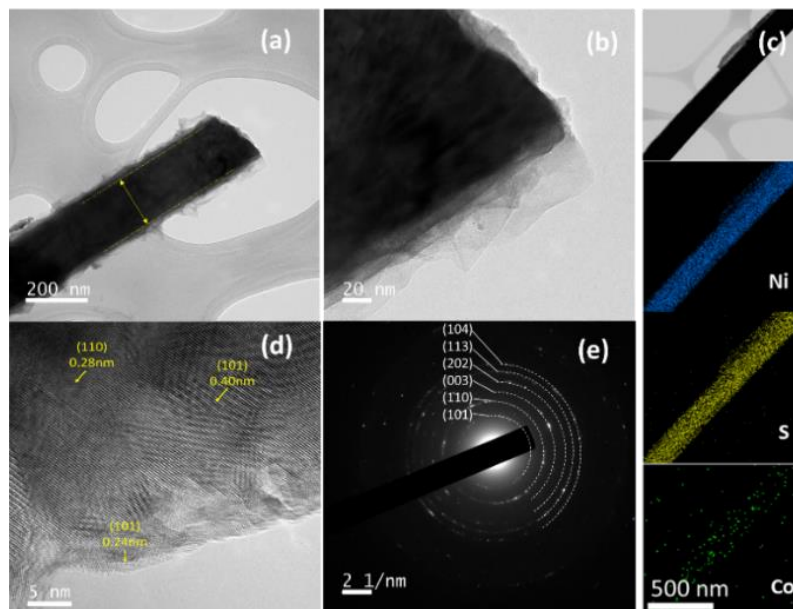
Figure 4. (**a**) Low and (**b**) high-magnification TEM images of the $Co_{0.5}$–Ni_3S_2 nanowire, (**c**) EDS mapping images, (**d**) lattice-resolved HRTEM image of the $Co_{0.5}$–Ni_3S_2 nanowire, and (**e**) SAED pattern of the $Co_{0.5}$–Ni_3S_2 nanowire.

Additional evidence regarding the chemical state of the as-synthesized $Co_{0.5}$–Ni_3S_2 electrode was obtained using XPS. The full survey spectrum (Figure 5a) of the $Co_{0.5}$–Ni_3S_2 electrode reveals that only Ni, Co, O, and C are present, with no other impurity peaks observed. The presence of Co and O is likely caused by the adsorption of $Co(OH)_2$ at the surface of the Ni_3S_2 nanowire, and the small C presence may be due to the reference and the exposure of the sample to the atmosphere [46]. The high-resolution spectrum of Ni 2p (Figure 5b) shows two main core levels of Ni $2p_{3/2}$ and Ni $2p_{1/2}$ that are characteristic of the Ni state are located at 855.1 and 872.8 eV, with two satellite peaks at 860.9 and 878.9 eV, respectively, indicating the formation of Ni^{2+} and Ni^{3+} [47–49]. To investigate the $Co(OH)_2$ shell formation on the surfaces of the Ni_3S_2 nanowires, the Co 2p XP spectrum was obtained, as shown in Figure 5c. Peaks representing Co $2p_{3/2}$ (780.4 and 774.0 eV) and Co $2p_{1/2}$ (796.5 and 796.0 eV) are observed. These peaks (796.0 and 780.4 eV) are attributed to Co^{2+}, indicating the formation of $Co(OH)_2$ [50–52]. For detailed insight into the presence of hydroxide, the O 1s spectrum of the $Co_{0.5}$–Ni_3S_2 electrode was analyzed, as shown in Figure 5d. The curve fitting of the O 1s spectrum indicates that the sample consists of two components, represented by peaks at 531.5 and 530.4 eV. The 531.5 eV peak indicates a bound hydroxide group (OH^-), confirming that $Co(OH)_2$ is successfully formed on the Ni_3S_2 surface [53,54]. The small peak at 530.4 eV indicates the H–O bonds in water [55–57]. Therefore, the XP spectra, when combined with the XRD and TEM results, indicate the successful preparation of the $Co(OH)_2$ shells on the surfaces of the Ni_3S_2 nanowire cores.
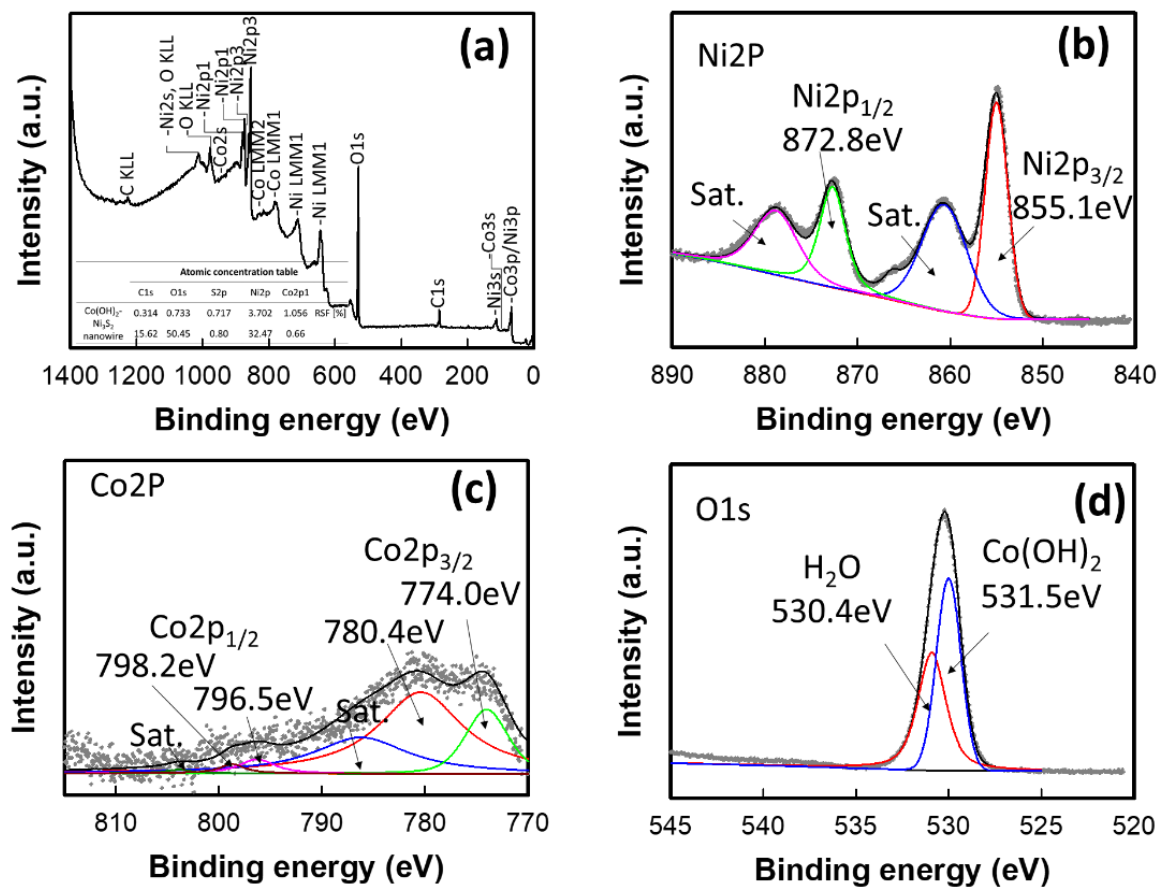
**Figure 5.** XPS spectra of the $Co_{0.5}$–Ni_3S_2 electrode. (**a**) Survey, (**b**) Ni 2p, (**c**) Co 2p, and (**d**) O 1s electron XPS spectra.

The electrochemical behaviors of the Ni_3S_2 and $Co(OH)_2$–Ni_3S_2 electrodes were initially investigated using CV (Figure 6a). For Ni_3S_2, redox peaks are observed at 0.20 and 0.30 V, respectively, indicating pseudocapacitive behavior [58]. Compared to those of Ni_3S_2, the redox peaks shift negatively in the voltammogram of $Co(OH)_2$–Ni_3S_2, indicating that the surface redox reactions of $Co^{2+}/Co^{3+}/Co^{4+}$ and Ni^{2+}/Ni^{3+} may facilitate OH^- transfer from the electrolyte [59,60]. The voltammogram of $Co_{0.5}$–Ni_3S_2 clearly shows a large integrated area, suggesting that the former exhibits a higher electrochemical capacitance. Figure 6b shows the CV of the $Co_{0.5}$–Ni_3S_2 electrode at scan rates ranging from 5 to 50 mV s^{-1}. The response current density increases linearly with increasing scan rate and the cathodic and cathodic current peaks are shifted more positively and negatively, respectively. However, as the scan rates increase, clear redox peaks are observed, indicating the slow electron or ion transfer kinetics of the interfacial redox reactions [61]. Conversely, the voltammograms of $Co_{0.5}$–Ni_3S_2 at scan rates of $\leq$20 mV s^{-1} retain their original shapes, and the currents are higher than that of Ni_3S_2, indicating the rapid kinetics of electron or ion transfer in the interfacial redox reactions [62]. Figure 6c shows the galvanostatic charge/discharge (GCD) curves of $Co_{0.5}$–Ni_3S_2 at different current densities. All GCD curves shows the clear voltage plateaus suggesting Faradaic redox reactions. The specific capacitance, SCs, (C_S, F g^{-1}) and area capacitances (C_A, F cm^{-2}) of the electrodes are calculated based on the GCD curves using the following equations [63]:

$$C_S = \frac{I \cdot \left(\frac{\Delta t}{\Delta V} \right)}{m} \tag{1}$$

$$C_A = \frac{I \cdot \left(\frac{\Delta t}{\Delta V} \right)}{A} \qquad (2)$$

where I, ΔV, Δt, m, and A denote the discharge current (mA), working potential window (V), discharging time (s), deposited mass of the active material (g), and area of the NF coated with the active material (1×1 cm^2), respectively.
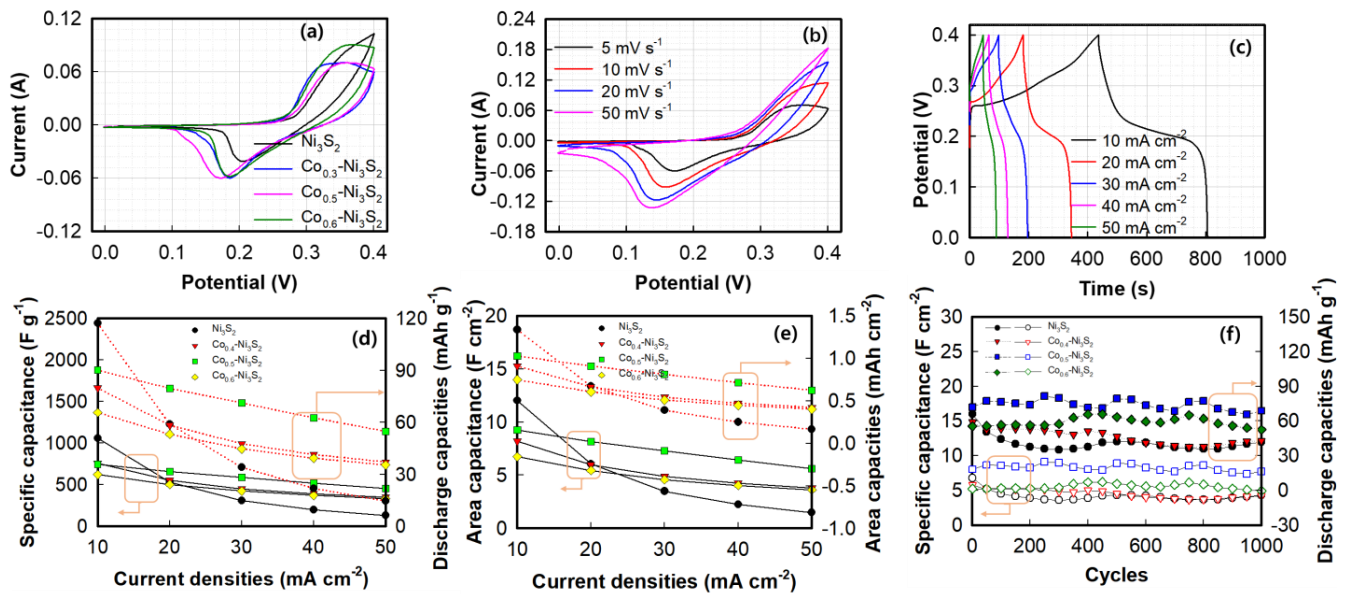
Figure 6. Cyclic voltammograms of (**a**) different electrodes at 5 mV s^{-1}, (**b**) Co$_{0.5}$–Ni$_3$S$_2$ at different scan rates, (**c**) galvanostatic charge–discharge of Co$_{0.5}$–Ni$_3$S$_2$ electrode, (**d**) specific capacitances and capacities, (**e**) area capacitances and capacities, and (**f**) cycling performances at 20 mA cm^{-2}.

Figure 6d,e shows the rate capabilities of various electrodes calculated during GCD. Co$_{0.5}$–Ni$_3$S$_2$ exhibits a very high SC compared to those of the other samples. The SC (plot with slid lines) is 742.6 F g^{-1} (9.25 F cm^{-2}) at a current density of 10 mA cm^{-2}, which declines to 451.8 F g^{-1} (5.63 F cm^{-2}) when the current density increases to 50 mA cm^{-2}. As shown in the GCD curve, the electrode materials of the Ni$_3$S$_2$ and Co-Ni$_3$S$_2$ shows the clearly redox plateau; therefore, the specific and area capacities (dotted lines) were also plotted in the Figure 6d,e. The discharge capacity of Co$_{0.5}$–Ni$_3$S$_2$ shows that the 90.1 mAh g^{-1} at a current density of 10 mA cm^{-2} and 52.8 mAh g^{-1} at 50 mA cm^{-2}. The high SC and capacity of Co$_{0.5}$–Ni$_3$S$_2$ may be due to the unique core–shell nanowires, wherein highly conductive Ni$_3$S$_2$ with a high SC is critical in enhancing the capacitance of Co(OH)$_2$ with an ultrathin nanosheet morphology. Figure 6f shows the cycling performances of Ni$_3$S$_2$ and Co–Ni$_3$S$_2$. Ni$_3$S$_2$ and Co$_{0.5}$–Ni$_3$S$_2$ showed retention rates of 83.7% and 95.4%, respectively, up to 1000 cycles, indicating that the core–shell structure improves the long–term electrochemical stability of the KOH electrolyte system. The optimal SC and cycling performance of the electroactive Ni$_3$S$_2$ electrode are superior or comparable to those of previously reported Ni$_3$S$_2$ electrodes (Table 1) [25,64–68].

The electrochemical performance of the AC electrode in the three–electrode configuration was measured, with the AC coated on a nickel mesh (1×1 cm^2) used as the working electrode. Figure 7 shows the electrochemical behavior of the AC electrode at different scan rates. The CV curves (Figure 7a) of the AC electrode reveal excellent symmetrical rectangular shapes at all scan rates. This is characteristic of an ideal EDLC material and suggests good charge propagation, rapid ion diffusion within the pores and reorganization of the electrical double layer, and low contact resistance [69]. Figure 7b,c show the GCD curves of the AC electrode at different current densities (10–50 mA cm^{-2}) and the rate capabilities, respectively. The charge–discharge curves of AC electrodes are linear and symmetrical, indicating the good reversibility. The SCs of the AC electrode are calculated

based on the GCD curves using Equation (1). An SC is 109.8 F g^{-1} (0.4 F cm^{-2}) appears at 5 mA cm^{-2}, which declines to 101.5 F g^{-1} (0.34 F cm^{-2}) at 50 mA cm^{-2}. The AC electrode maintains 99.5% of its initial capacitance after 2000 cycles as shown in Figure 6d.

Table 1. Comparison of the electrochemical energy storage performances observed in this study with those of previously reported Ni$_3$S$_2$ electrodes.

Electrodes	Current Density	Specific or Areal Capacitance	Cycle Stability	Ref.
Ni$_3$S$_2$	15 A g^{-1}	670 F g^{-1}	97.4% (2000)	[50]
Ni$_3$S$_2$ nanosheet @ Ni$_3$S$_2$ nanorods	20.6 A g^{-1}	489 F g^{-1}	89.3% (5000)	[51]
Ni$_3$S$_2$ nanoflake	50 A cm^{-2}	2.28 F cm^{-2}	77% (5000)	[52]
Ni$_3$S$_2$ nanoporous	1 mA cm^{-2}	3.42 F cm^{-2}	102% (4250)	[53]
Ni$_3$S$_2$ nanosheet	15 mA cm^{-2}	1.342 F cm^{-2}	93.6% (3000)	[54]
Ni$_3$S$_2$ nest	25 mA cm^{-2}	682.9 F g^{-1}	69% (1000)	[55]
Ni$_3$S$_2$ nanowire	20 mA cm^{-2}	530.3 F g^{-1} (6.05 F cm^{-2})	83.7% (1000)	This study
Co(OH)$_2$–Ni$_3$S$_2$ nanowire	20 mA cm^{-2}	656.2 F g^{-1} (8.17 F cm^{-2})	95.4% (1000)	
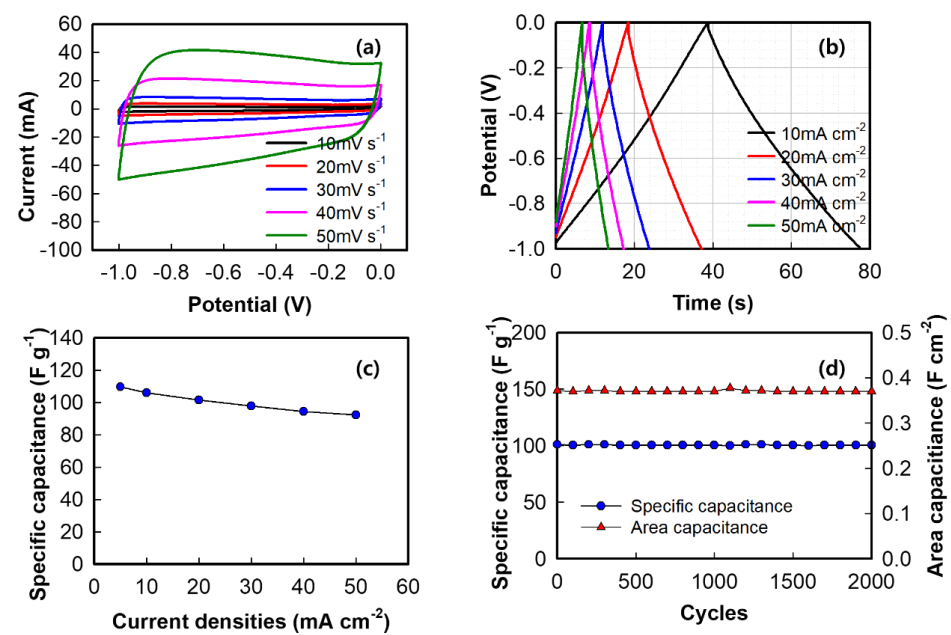
Figure 7. (**a**) Cyclic voltammograms of the AC negative electrode at 10–50 mV s^{-1}, (**b**) galvanostatic charge–discharge curves of the AC electrode at 10–50 mA cm^{-2}, (**c**) specific capacitances at different current densities, and (**d**) cycling performance of the AC electrode at 20 mA cm^{-2}.

The ASC device was assembled in a two-electrode configuration using a Co$_{0.5}$–Ni$_3$S$_2$ positive electrode and an AC negative electrode. Prior to assembling the ASC device, the mass balance of the positive and negative electrodes was determined. The mass (m) of the positive and negative electrodes was determined by Equation (3) [70]:

$$\frac{m_+}{m_-} = \frac{C_- \times \Delta V_-}{C_+ \times \Delta V_+} \tag{3}$$

where *m*, *C*, and ΔV are the masses, SCs, and potential windows of the Co$_{0.5}$–Ni$_3$S$_2$ positive (+) and AC negative (−) electrodes, in a typical three–electrode configuration. The mass ratio of AC and Co$_{0.5}$–Ni$_3$S$_2$ is 2.73:1. The SC of the device was calculated using Equation (1), where m is the sum of the deposited masses of Co$_{0.5}$–Ni$_3$S$_2$ and AC (cathode and anode

materials, respectively). The total active mass is 27 mg. The potential window of the $Co_{0.5}$–Ni_3S_2//AC device is obtained from the cyclic voltammograms of $Co_{0.5}$–Ni_3S_2 (Figure 6b) and AC (Figure 7a) in a three–electrode cell. AC exhibits the typical EDLC pattern in the potential range from −1.0–0.0 V and $Co_{0.5}$–Ni_3S_2 exhibits the potential range 0–0.4 V. Based on the cyclic voltammograms of the $Co_{0.5}$–Ni_3S_2 and AC electrodes, the potential window of the ASC device may be extended to 1.6 V [71].

The cyclic voltammograms exhibit large current areas with broad redox peaks, which are typical of asymmetric supercapacitors that combine electrochemical capacitors and EDLC properties [72]. The potential window of the $Co_{0.5}$–Ni_3S_2//AC device was again confirmed using CV at different windows. As shown in Figure 8a, no clear polarization is observed in the voltage range 0.0–1.60 V, indicating that 1.40 V is a reasonable potential window limit for this ASC in 3.0 M KOH electrolyte. Therefore, the combined working potential of the ASC is 1.6 V. Figure 8b shows the CV of the ASC at different scan rates in the potential window 0–1.6 V. The CV exhibit broad redox peaks, which are associated with the pseudocapacitive Ni_3S_2 and AC, indicating the ideal capacitive behavior of the device [73]. Figure 8c shows the typical GCD curves of the ASC with observed SCs of 2.37 F cm^{-2} (58.41 F g^{-1}) at 20 mA cm^{-2}. In addition, the SC retention of the ASC device is 94% at 20 mA cm^{-2}, as shown in the inset of Figure 8c. To study the interfacial charge transfer resistance of the supercapacitor with the $Co_{0.5}$–Ni_3S_2//AC device, EIS was performed after the 1st and 1000th discharges, as shown in Figure 8d. The Nyquist plot in the high–frequency region reveals that the electronic resistance of the device, also denoted the solution resistance (R_S), is the equivalent series resistance (ESR), which describes the resistance of the electrolyte combined with the internal resistance of the electrode [74]. The semicircle is the result of the double-layer charging of the AC electrode and the Faradaic reaction of the $Co_{0.5}$–Ni_3S_2 electrode. The slope of the curve in the low-frequency region corresponds to the Warburg element, which represents the electrolyte diffusion within the porous electrode and proton diffusion within the host material [75,76]. The Nyquist plot was fitted using the Randles equivalent circuit, as shown in the inset of Figure 8d, using the NOVA program, where R_{ct} is the electrode-electrolyte charge transfer resistance, R_L is the leakage resistance, C_L is the double–layer capacitance, CPE_{DL} is the constant phase element of the double layer, and CPE_L is the mass capacitance. The ESR of the asymmetric device decreases from 0.25 to 0.22 Ω after 1000 cycles, and R_{ct} also decreases after 1000 cycles, suggesting a significant decrease in the R_S and R_{ct} due to the increased surface area available during repeated cycling, which may improve the supercapacitor performance [77].

The $Co_{0.5}$–Ni_3S_2//AC asymmetric device exhibits a maximum energy density of 60.3 W h kg^{-1} (20 mA cm^{-2}) at a power density of 1944.3 W kg^{-1} (50 mA cm^{-2}) and 36.0 W h kg^{-1} at a power density of 4309 W kg^{-1}. The energy (*E*, W h kg^{-1}) and power densities (*P*, W kg^{-1}) are calculated based on the discharge curve using Equations (4) and (5), respectively [78]:

$$E = \frac{I \int V dt}{m \times 3.6} \tag{4}$$

$$P = \frac{E \times 3600}{t} \tag{5}$$

where, *I*, $\int V dt$, *m*, and *t* are the discharge current (mA), integral area under the discharge curve, masses, and discharging time (s), respectively. The results are comparable or even superior to those of previously reported supercapacitors (Table 2), such as the rGO@Ni_3S_2//AC (37.19 W h kg^{-1} at 399.9 W kg^{-1}), Ni_3S_2//AC (36 W h kg^{-1} at 400 W kg^{-1}), and Ni_3S_2@CoS//AC (23.69 W h kg^{-1} at 268.95 W kg^{-1}) devices [66,79–85]. A comparison of these results based on power and energy densities with related reported devices is also summarized. To further evaluate the practical applications of the $Co_{0.5}$–Ni_3S_2//AC asymmetric device, the assembled device easily powers an LED after charging, as shown in the inset of Figure 8c. The $Co_{0.5}$–Ni_3S_2//AC asymmetric device exhibits consid-

erable potential for use in next–generation flexible energy storage devices, for applications in smart, wearable electronics.
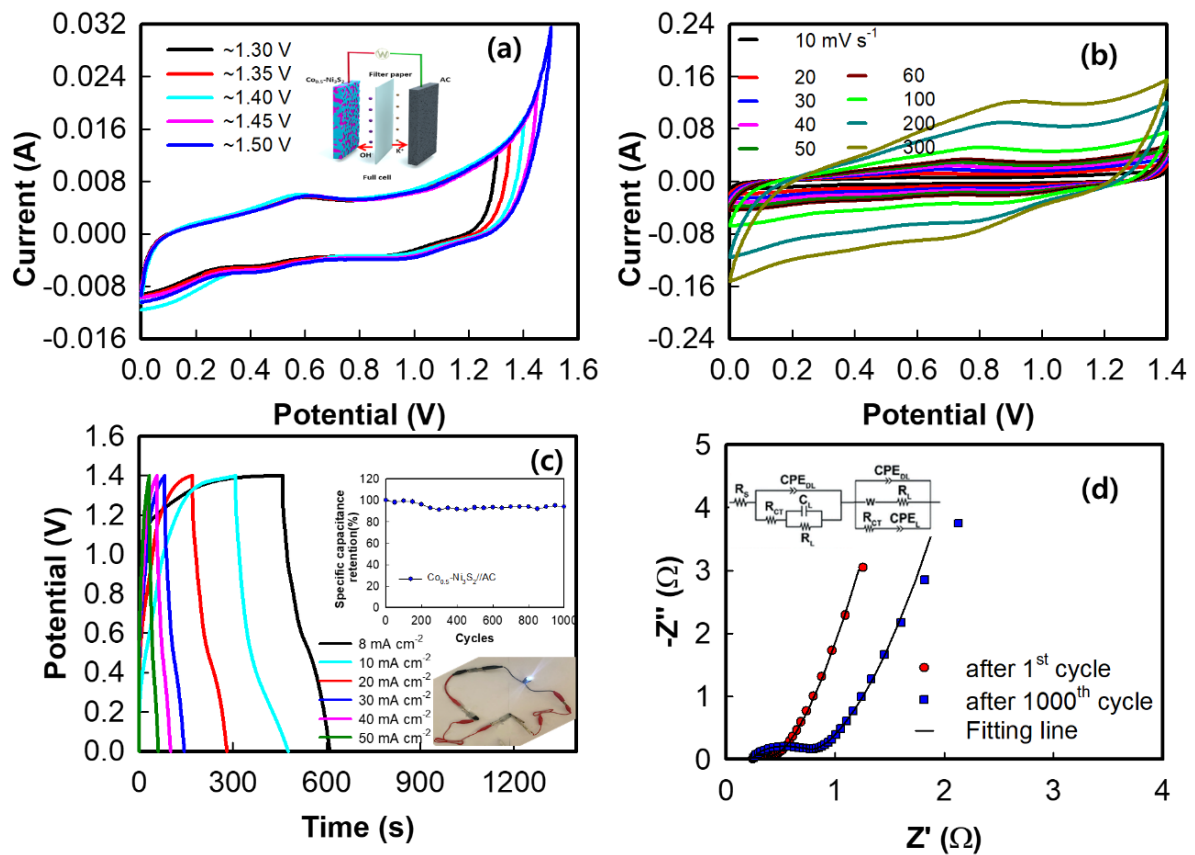
Figure 8. Cyclic voltammograms of the $Co_{0.5}$–Ni_3S_2//AC device (**a**) in different voltage windows and (**b**) at different scan rates. (**c**) Galvanostatic charge–discharge curves of the $Co_{0.5}$–Ni_3S_2//AC device at 8–50 mA cm^{-2} and (inset) cycle retention at 20 mA cm^{-2}, and (**d**) EIS and fitting results of the $Co_{0.5}$–Ni_3S_2//AC device after 1 and 1000 cycles.

Table 2. Comparison of the electrochemical energy storage performance observed in this study with those of previously reported asymmetric devices based on Ni_3S_2 and AC electrodes [66,79–85].

Electrodes	Energy Density (W h kg^{-1})	Power Density (W kg^{-1})	Ref.
rGO–Ni_3S_2//AC	37.19	399.9	[66]
Ni_3S_2//AC	36	400	[79]
Ni_3S_2@CoS//AC	23.69	268.95	[80]
Ni_3S_2//AC	10.01	150.12	[80]
Ni_3S_2/MWCNT–NC//AC	19.8	798	[81]
C@MnNiCo–OH/Ni_3S_2/NF//AC	36,000	799.95	[82]
Ni_3S_2@PPy//AC	17.54	179.33	[83]
Ni_3S_2//AC	17.73	179.32	[83]
NiSe/Ni_3S_2//AC	38.7	192	[84]
(Ni_3S_2/Ni@CC//AC/CC	0.27 W h cm^{-2}	4.90 W cm^{-2}	[85]
Co(OH)$_2$–Ni_3S_2 nanowire	60.3	1944.3	This study

4. Conclusions

Ni_3S_2 and $Co(OH)_2$ shell-coated Ni_3S_2 nanowires were successfully prepared using a facile one–step hydrothermal reaction as positive electrodes for use in supercapacitors. The Ni_3S_2 nanowires were uniformly formed on the smooth NF surface, and the $Co(OH)_2$ shell was uniformly formed on the Ni_3S_2 nanowire surface. As NF participates directly as the nickel source, Ni_3S_2 was formed more closely to the NF surface, and the $Co(OH)_2$ shell suppressed the loss of active material during charging–discharging. The 0.5 mmol $Co(OH)_2$ shell–coated $Co_{0.5}$–Ni_3S_2 electrode exhibited superior performance, with a high discharge capacity of 1837 F g^{-1} (16.07 F cm^{-2}) at a current density of 5 mA cm^{-2}, and maintained a satisfactory rate capability of 583 F g^{-1} (16.07 F cm^{-2}) at a much higher current density of 50 mA cm^{-2}. The ASC delivers a power density as high as 1036 W kg^{-1} at an energy density of 43 W h kg^{-1}, with a good cycling stability of 92%, which reveals its suitability for use in numerous energy storage applications. Therefore, the core–shell architecture developed in this study is an efficient way to improve the electrochemical performances in various promising energy storage applications.

Author Contributions: Conceptualization, E.M.J.; methodology, X.L.W.; investigation, X.L.W. and J.C.; data curation, X.L.W.; writing, E.M.J.; review and editing, P.B. and B.J.; visualization, supervision, project administration, and funding acquisition, S.M.J. All authors have read and agreed to the published version of the manuscript.

Institutional Review Board Statement: Not applicable.

Informed Consent Statement: Not applicable.

Data Availability Statement: Not applicable.

Conflicts of Interest: The authors declare no conflict of interest.

References

1. Huang, S.; Zhu, X.; Sarkar, S.; Zhao, Y. Challenges and opportunities for supercapacitors. *APL Mater.* **2019**, *7*, 100901. [CrossRef]
2. Abdel Maksoud, M.I.A.; Fahim, R.A.; Shalan, A.E.; Abd Elkodous, M.; Olojede, S.O.; Osman, A.I.; Farrell, C.; Al-Muhtaseb, A.a.H.; Awed, A.S.; Ashour, A.H.; et al. Advanced materials and technologies for supercapacitors used in energy conversion and storage: A review. *Environ. Chem. Lett.* **2020**, *19*, 375–439. [CrossRef]
3. Lee, S.-H.; Kim, K.-Y.; Yoon, J.-R. Binder- and conductive additive-free laser-induced graphene/$LiNi_{1/3}Mn_{1/3}Co_{1/3}O_2$ for advanced hybrid supercapacitors. *NPG Asia Mater.* **2020**, *12*, 28. [CrossRef]
4. Lamb, J.J.; Burheim, O.S. Lithium-ion capacitors: A review of design and active materials. *Energies* **2021**, *14*, 979. [CrossRef]
5. Sung, J.; Shin, C. Recent studies on supercapacitors with next-generation structures. *Micromachines* **2020**, *11*, 1125. [CrossRef]
6. Simon, P.; Gogotsi, Y. Materials for electrochemical capacitors. *Nat. Mater.* **2008**, *7*, 845–854. [CrossRef]
7. Obreja, V.V.N. Supercapacitors specialities-Materials review. *AIP Conf. Proc.* **2014**, *98*, 1597. [CrossRef]
8. Danilovic, N.; Subbaraman, R.; Chang, K.C.; Chang, S.H.; Kang, Y.J.; Snyder, J.; Paulikas, A.P.; Strmcnik, D.; Kim, Y.T.; Myers, D.; et al. Activity-stability trends for the oxygen evolution reaction on monometallic oxides in acidic environments. *J. Phys. Chem. Lett.* **2014**, *5*, 2474–2478. [CrossRef]
9. Branco, J.B.; Ferreira, A.C.; Vieira, F.; Martinho, J.F. Cerium-based bimetallic oxides as catalysts for the methanation of CO_2: Influence of the preparation method. *Energy Fuels* **2021**, *35*, 6725–6737. [CrossRef]
10. Anantharaj, S.; Karthick, K.; Kundu, S. Evolution of layered double hydroxides (LDH) as high performance water oxidation electrocatalysts: A review with insights on structure, activity and mechanism. *Mater. Today Energy* **2017**, *6*, 1–26. [CrossRef]
11. Wang, A.; Wang, H.; Zhang, S.; Mao, C.; Song, J.; Niu, H.; Jin, B.; Tian, Y. Controlled synthesis of nickel sulfide/graphene oxide nanocomposite for high-performance supercapacitor. *Appl. Surf. Sci.* **2013**, *282*, 704–708. [CrossRef]
12. Santhosh, N.M.; Upadhyay, K.K.; Strazar, P.; Filipic, G.; Zavasnik, J.; Mao de Ferro, A.; Silva, R.P.; Tatarova, E.; Montemor, M.F.; Cvelbar, U. Advanced carbon-nickel sulfide hybrid nanostructures: Extending the limits of battery-type electrodes for redox-based supercapacitor applications. *ACS Appl Mater Interfaces* **2021**, *13*, 20559–20572. [CrossRef]
13. Wang, H.; Wang, J.; Liang, M.; He, Z.; Li, K.; Song, W.; Tian, S.; Duan, W.; Zhao, Y.; Miao, Z. Novel dealloying-fabricated NiS/NiO nanoparticles with superior cycling stability for supercapacitors. *ACS Omega* **2021**, *6*, 17999–18007. [CrossRef]

14. Huang, H.; Deng, X.; Yan, L.; Wei, G.; Zhou, W.; Liang, X.; Guo, J. One-step synthesis of self-supported Ni_3S_2/NiS composite film on Ni foam by electrodeposition for high-performance supercapacitors. *Nanomaterials* **2019**, *9*, 1718. [CrossRef]

15. Lin, J.-Y.; Tai, S.-Y.; Chou, S.-W. Bifunctional one-dimensional hierarchical nanostructures composed of cobalt sulfide nanoclusters on carbon nanotubes backbone for dye-sensitized solar cells and supercapacitors. *J. Phys. Chem. C* **2013**, *118*, 823–830. [CrossRef]

16. Luo, Y.; Yang, C.; Tian, Y.; Tang, Y.; Yin, X.; Que, W. A long cycle life asymmetric supercapacitor based on advanced nickel-sulfide/titanium carbide (MXene) nanohybrid and MXene electrodes. *J. Power Sources* **2020**, *450*, 227694. [CrossRef]

17. Shombe, G.B.; Khan, M.D.; Zequine, C.; Zhao, C.; Gupta, R.K.; Revaprasadu, N. Direct solvent free synthesis of bare alpha-NiS, beta-NiS and alpha-beta-NiS composite as excellent electrocatalysts: Effect of self-capping on supercapacitance and overall water splitting activity. *Sci Rep.* **2020**, *10*, 3260. [CrossRef]

18. Jiang, N.; Tang, Q.; Sheng, M.; You, B.; Jiang, D.-E.; Sun, Y. Nickel sulfides for electrocatalytic hydrogen evolution under alkaline conditions: A case study of crystalline NiS, NiS_2, and Ni_3S_2 nanoparticles. *Catal. Sci. Technol.* **2016**, *6*, 1077–1084. [CrossRef]

19. Tang, J.; Ni, S.; Chao, D.; Liu, J.; Yang, X.; Zhao, J. High-rate and ultra-stable Na-ion storage for Ni_3S_2 nanoarrays via self-adaptive pseudocapacitance. *Electrochim. Acta* **2018**, *265*, 709–716. [CrossRef]

20. Darezereshki, E.; Vakylabad, A.B.; Hassanzadeh, A.; Niedoba, T.; Surowiak, A.; Koohestani, B. Hydrometallurgical synthesis of nickel nano-sulfides from spent lithium-ion batteries. *Minerals* **2021**, *11*, 419. [CrossRef]

21. Lai, C.-H.; Huang, K.-W.; Cheng, J.-H.; Lee, C.-Y.; Lee, W.-F.; Huang, C.-T.; Hwang, B.-J.; Chen, L.-J. Oriented growth of large-scale nickel sulfide nanowire arrays via a general solution route for lithium-ion battery cathode applications. *J. Mater. Chem.* **2009**, *19*, 7277–7283. [CrossRef]

22. Zhu, X.; Wen, Z.; Gu, Z.; Huang, S. Room-temperature mechanosynthesis of Ni_3S_2 as cathode material for rechargeable lithium polymer batteries. *J. Electrochem. Soc.* **2006**, *153*, A504–A507. [CrossRef]

23. Takeuchi, T.; Sakaebe, H.; Kageyama, H.; Sakai, T.; Tatsumi, K. Preparation of NiS_2 using spark-plasma-sintering process and its electrochemical properties. *J. Electrochem. Soc.* **2008**, *155*, A679–A684. [CrossRef]

24. Chou, S.-W.; Lin, J.-Y. Cathodic Deposition of flaky nickel sulfide nanostructure as an electroactive material for high-performance supercapacitors. *J. Electrochem. Soc.* **2013**, *160*, D178–D182. [CrossRef]

25. Krishnamoorthy, K.; Gk, V.; Radhakrishnan, S.; Kim, S. Corrigendum to "One pot hydrothermal growth of hierarchical nanos-tructured Ni_3S_2 on Ni foam for supercapacitor application" [Chem. Eng. J. 251 (2014) 116–122]. *Chem. Eng. J.* **2015**, *266*, 386. [CrossRef]

26. Zhang, Y.; Zhang, J.; Ding, D.; Gao, Y. Controllable synthesis of three-dimensional beta-NiS nanostructured assembly for hybrid-type asymmetric supercapacitors. *Nanomaterials* **2020**, *10*, 487. [CrossRef]

27. Hu, Q.; Zhang, S.; Zou, X.; Hao, J.; Bai, Y.; Yan, L.; Li, W. Coordination agent-dominated phase control of nickel sulfide for high-performance hybrid supercapacitor. *J. Colloid. Interface Sci.* **2021**, *607*, 45–52. [CrossRef]

28. Sajjad, M.; Khan, Y. Rational design of self-supported Ni_3S_2 nanoparticles as a battery type electrode material for high-voltage (1.8 V) symmetric supercapacitor applications. *Cryst. Eng. Commun.* **2021**, *23*, 2869–2879. [CrossRef]

29. Wu, Z.; Huang, H.; Xiong, W.; Yang, S.; Huang, H.; Zou, Y.; Zhou, W.; Cheng, Z.; Wang, J.; Luo, G. One-pot synthesis of glucose-derived carbon coated Ni_3S_2 nanowires as a battery-type electrode for high performance supercapacitors. *Nanomaterials* **2021**, *11*, 678. [CrossRef]

30. Phonsuksawang, P.; Khajondetchairit, P.; Ngamchuea, K.; Butburee, T.; Sattayaporn, S.; Chanlek, N.; Suthirakun, S.; Siritanon, T. Enhancing performance of $NiCo_2S_4$/Ni_3S_2 supercapacitor electrode by Mn doping. *Electrochim. Acta* **2021**, *368*, 137634. [CrossRef]

31. Shinde, N.M.; Xia, Q.X.; Shinde, P.V.; Yun, J.M.; Mane, R.S.; Kim, K.H. Sulphur source-inspired self-grown 3D Ni_xS_y nanostructures and their electrochemical supercapacitors. *ACS Appl. Mater. Interfaces* **2019**, *11*, 4551–4559. [CrossRef] [PubMed]

32. Vidhya, M.S.; Ravi, G.; Yuvakkumar, R.; Velauthapillai, D.; Thambidurai, M.; Dang, C.; Saravanakumar, B. Nickel–cobalt hydroxide: A positive electrode for supercapacitor applications. *RSC Adv.* **2020**, *10*, 19410–19418. [CrossRef]

33. Kumar, R.; Singh, R.K.; Savu, R.; Dubey, P.K.; Kumar, P.; Moshkalev, S.A. Microwave-assisted synthesis of void-induced graphene-wrapped nickel oxide hybrids for supercapacitor applications. *RSC Adv.* **2016**, *6*, 26612–26620. [CrossRef]

34. Vishnukumar, P.; Saravanakumar, B.; Ravi, G.; Ganesh, V.; Guduru, R.K.; Yuvakkumar, R. Synthesis and characterization of NiO/$Ni_3V_2O_8$ nanocomposite for supercapacitor applications. *Mater. Lett.* **2018**, *219*, 114–118. [CrossRef]

35. Anil Kumar, Y.; Dasha Kumar, K.; Kim, H.J. A novel electrode for supercapacitors: Efficient PVP-assisted synthesis of Ni_3S_2 nanostructures grown on Ni foam for energy storage. *Dalton Trans.* **2020**, *49*, 4050–4059. [CrossRef] [PubMed]

36. Wu, B.; Qian, H.; Nie, Z.; Luo, Z.; Wu, Z.; Liu, P.; He, H.; Wu, J.; Chen, S.; Zhang, F. Ni_3S_2 nanorods growing directly on Ni foam for all-solid-state asymmetric supercapacitor and efficient overall water splitting. *J. Energy Chem.* **2020**, *46*, 178–186. [CrossRef]

37. Chen, F.; Wang, H.; Ji, S.; Linkov, V.; Wang, R. Core-shell structured Ni_3S_2@$Co(OH)_2$ nano-wires grown on Ni foam as binder-free electrode for asymmetric supercapacitors. *Chem. Eng. J.* **2018**, *345*, 48–57. [CrossRef]

38. Wang, X.; Shi, B.; Fang, Y.; Rong, F.; Huang, F.; Que, R.; Shao, M. High capacitance and rate capability of a Ni_3S_2@CdS core–shell nanostructure supercapacitor. *J. Mater. Chem. A* **2017**, *5*, 7165–7172. [CrossRef]

39. Wang, J.; Chao, D.; Liu, J.; Li, L.; Lai, L.; Lin, J.; Shen, Z. Ni_3S_2@MoS_2 Core/shell nanorod arrays on Ni foam for high-performance electrochemical energy storage. *Nano Energy* **2014**, *7*. [CrossRef]

40. Liu, X.X.; Wu, R.; Wang, Y.; Xiao, S.H.; He, Q.; Niu, X.B.; Blackwood, D.J.; Chen, J.S. Self-supported core/shell Co_3O_4@Ni_3S_2 nanowires for high-performance supercapacitors. *Electrochim. Acta* **2019**, *311*, 221–229. [CrossRef]

41.   Tronganh, N.; Gao, Y.; Jiang, W.; Tao, H.; Wang, S.; Zhao, B.; Jiang, Y.; Chen, Z.; Jiao, Z. Hierarchically assembled 3D nanoflowers and 0D nanoparticles of nickel sulfides on reduced graphene oxide with excellent lithium storage performances. *Appl. Surf. Sci.* **2018**, *439*, 386–393. [CrossRef]

42.   Tian, Y.; Wang, Q.; Peng, Z.; Guan, S.; Fu, X. Ni Foam-supported tin oxide nanowall array: An integrated supercapacitor anode. *Molecules* **2021**, *26*, 4517. [CrossRef] [PubMed]

43.   Yuan, R.; Jiang, M.; Gao, S.; Wang, Z.; Wang, H.; Boczkaj, G.; Liu, Z.; Ma, J.; Li, Z. 3D mesoporous α-Co(OH)$_2$ nanosheets electrodeposited on nickel foam: A new generation of macroscopic cobalt-based hybrid for peroxymonosulfate activation. *Chem. Eng. J.* **2020**, *380*, 122447. [CrossRef]

44.   Yang, H.; Long, Y.; Zhu, Y.; Zhao, Z.; Ma, P.; Jin, J.; Ma, J. Crystal lattice distortion in ultrathin Co(OH)$_2$ nanosheets inducing elongated Co–OOH bonds for highly efficient oxygen evolution reaction. *Green Chem.* **2017**, *19*, 5809–5817. [CrossRef]

45.   Zhang, J.; Lin, J.; Wu, J.; Xu, R.; Lai, M.; Gong, C.; Chen, X.; Zhou, P. Excellent electrochemical performance hierarchical Co$_3$O$_4$@Ni$_3$S$_2$ core/shell nanowire arrays for asymmetric supercapacitors. *Electrochim. Acta* **2016**, *207*, 87–96. [CrossRef]

46.   Zhang, X.; Zhang, S.; Li, J.; Wang, E. One-step synthesis of well-structured NiS-Ni$_2$P$_2$S$_6$ nanosheets on nickel foam for efficient overall water splitting. *J. Mater. Chem. A* **2017**, *5*, 22131–22136. [CrossRef]

47.   Zhou, Y.; Li, T.; Xi, S.; He, C.; Yang, X.; Wu, H. One-step synthesis of self-standing Ni$_3$S$_2$/Ni$_2$P heteronanorods on nickel foam for efficient electrocatalytic hydrogen evolution over a wide pH range. *Chem. Cat. Chem.* **2018**, *10*, 5487–5495. [CrossRef]

48.   Jing, F.; Lv, Q.; Xiao, J.; Wang, Q.; Wang, S. Highly active and dual-function self-supported multiphase NiS–NiS$_2$–Ni$_3$S$_2$/NF electrodes for overall water splitting. *J. Mater. Chem. A* **2018**, *6*, 14207–14214. [CrossRef]

49.   Deng, S.; Zhang, K.; Xie, D.; Zhang, Y.; Zhang, Y.; Wang, Y.; Wu, J.; Wang, X.; Fan, H.J.; Xia, X.; et al. Correction to: High-index-faceted Ni$_3$S$_2$ branch arrays as bifunctional electrocatalysts for efficient water splitting. *Nanomicro Lett.* **2020**, *13*, 16. [CrossRef]

50.   Fu, Z.; Wang, Y.; Zhang, Y.; Qin, Q. Electrochemical reaction of nanocrystalline Co$_3$O$_4$ thin film with Lithium. *Solid State Ion.* **2004**, *170*, 105–109. [CrossRef]

51.   Wang, Y.; Hao, J.; Li, W.; Zuo, X.; Xiang, B.; Qiang, Y.; Zou, X.; Tan, B.; Hu, Q.; Chen, F. Mn$_3$O$_4$/Co(OH)$_2$ cactus-type nanoarrays for high-energy-density asymmetric supercapacitors. *J. Mater. Sci.* **2019**, *55*, 724–737. [CrossRef]

52.   Petitto, S.C.; Marsh, E.M.; Carson, G.A.; Langell, M.A. Cobalt oxide surface chemistry: The interaction of CoO(100), Co$_3$O$_4$(110) and Co$_3$O$_4$(111) with oxygen and water. *J. Mol. Catal. A Chem.* **2008**, *281*, 49–58. [CrossRef]

53.   Sayeed, M.A.; Herd, T.; O'Mullane, A.P. Direct electrochemical formation of nanostructured amorphous Co(OH)$_2$ on gold electrodes with enhanced activity for the oxygen evolution reaction. *J. Mater. Chem. A* **2016**, *4*, 991–999. [CrossRef]

54.   Shackery, I.; Patil, U.; Pezeshki, A.; Shinde, N.M.; Im, S.; Jun, S.C. Enhanced Non-enzymatic amperometric sensing of glucose using Co(OH)$_2$ nanorods deposited on a three dimensional graphene network as an electrode material. *Microchim. Acta* **2016**, *183*, 2473–2479. [CrossRef]

55.   Wang, J.; Xie, T.; Deng, Q.; Wang, Y.; Zhu, Q.; Liu, S. Three-dimensional interconnected Co(OH)$_2$ nanosheets on Ti mesh as a highly sensitive electrochemical sensor for hydrazine detection. *New J. Chem.* **2019**, *43*, 3218–3225. [CrossRef]

56.   Feng, S.; Liu, C.; Chai, Z.; Li, Q.; Xu, D. Cobalt-based hydroxide nanoparticles @ N-doping carbonic frameworks core–shell structures as highly efficient bifunctional electrocatalysts for oxygen evolution and oxygen reduction reactions. *Nano Res.* **2018**, *11*, 1482–1489. [CrossRef]

57.   Li, H.B.; Yu, M.H.; Lu, X.H.; Liu, P.; Liang, Y.; Xiao, J.; Tong, Y.X.; Yang, G.W. Amorphous cobalt hydroxide with superior pseudocapacitive performance. *ACS Appl. Mater Interfaces* **2014**, *6*, 745–749. [CrossRef]

58.   Kandula, S.; Shrestha, K.R.; Kim, N.H.; Lee, J.H. Fabrication of a 3D hierarchical sandwich Co$_9$S$_8$ /alpha-MnS@N-C@MoS$_2$ nanowire architectures as advanced electrode material for high performance hybrid supercapacitors. *Small* **2018**, *14*, e1800291. [CrossRef]

59.   Ye, L.; Zhao, L.; Zhang, H.; Zan, P.; Gen, S.; Shi, W.; Han, B.; Sun, H.; Yang, X.; Xu, T. Serpent-cactus-like Co-doped Ni(OH)$_2$/Ni$_3$S$_2$ hierarchical structure composed of ultrathin nanosheets for use in efficient asymmetric supercapacitors. *J. Mater. Chem. A* **2017**, *5*, 1603–1613. [CrossRef]

60.   Ali Akbari, M.S.; Bagheri, R.; Song, Z.; Najafpour, M.M. Oxygen-evolution reaction by nickel/nickel oxide interface in the presence of ferrate(VI). *Sci Rep.* **2020**, *10*, 8757. [CrossRef]

61.   Yadav, N.; Yadav, N.; Singh, M.K.; Hashmi, S.A. Nonaqueous, redox-active gel polymer electrolyte for high-performance supercapacitor. *Energy Technol.* **2019**, *7*, 1900132. [CrossRef]

62.   He, L.; Wang, Y.; Xu, Y.; Cai, W.; Zhu, M.; Wang, H. Facile synthesis of core-shell NiSe@α-Ni(OH)$_2$ as battery-type electrode for high-performance hybrid supercapacitor. *J. Alloys Compd.* **2021**, *876*, 160164. [CrossRef]

63.   Wang, S.; Xu, L.; Lu, W. Synergistic effect: Hierarchical Ni$_3$S$_2$@Co(OH)$_2$ heterostructure as efficient bifunctional electrocatalyst for overall water splitting. *Appl. Surf. Sci.* **2018**, *457*, 156–163. [CrossRef]

64.   Li, W.; Wang, S.; Xin, L.; Wu, M.; Lou, X. Single-crystal β-NiS nanorod arrays with a hollow-structured Ni$_3$S$_2$ framework for supercapacitor applications. *J. Mater. Chem. A* **2016**, *4*, 7700–7709. [CrossRef]

65.   Yilmaz, G.; Lu, X. Direct growth of 3D hierarchical porous Ni$_3$S$_2$ nanostructures on nickel foam for high-Performance supercapacitors. *ChemNanoMat* **2016**, *2*, 719–725. [CrossRef]

66.   Lin, H.; Liu, F.; Wang, X.; Ai, Y.; Yao, Z.; Chu, L.; Han, S.; Zhuang, X. Graphene-coupled flower-like Ni$_3$S$_2$ for a free-standing 3D aerogel with an ultra-high electrochemical capacity. *Electrochim. Acta* **2016**, *191*, 705–715. [CrossRef]

67. Zhuo, M.; Zhang, P.; Chen, Y.; Li, Q. Facile construction of graphene-like Ni_3S_2 nanosheets through the hydrothermally assisted sulfurization of nickel foam and their application as self-supported electrodes for supercapacitors. *RSC Adv.* **2015**, *5*, 25446–25449. [CrossRef]

68. Yang, J.; Guo, W.; Li, D.; Wei, C.; Fan, H.; Wu, L.; Zheng, W. Synthesis and electrochemical performances of novel hierarchical flower-like nickel sulfide with tunable number of composed nanoplates. *J. Power Sources* **2014**, *268*, 113–120. [CrossRef]

69. Liu, D.; Zhao, X.; Su, R.; Hao, Z.; Jia, B.; Li, S.; Dong, L. Highly porous graphitic activated carbons from lignite via microwave pretreatment and iron-catalyzed graphitization at low-temperature for supercapacitor electrode materials. *Processes* **2019**, *7*, 300. [CrossRef]

70. Wei, W.; Cui, X.; Chen, W.; Ivey, D.G. Manganese oxide-based materials as electrochemical supercapacitor electrodes. *Chem. Soc. Rev.* **2011**, *40*, 1697–1721. [CrossRef]

71. Zhuoqing, C.; Li, T.; Li, G.; Wang, K. One-pot in-situ synthesis of $Ni(OH)_2$–$NiFe_2O_4$ nanosheet arrays on nickel foam as binder-free electrodes for supercapacitors. *J. Mater. Sci. Mater. Electron.* **2019**, *30*, 600–608. [CrossRef]

72. Li, R.; Wang, S.; Huang, Z.; Lu, F.; He, T. $NiCo_2S_4$@$Co(OH)_2$ core-shell nanotube arrays in situ grown on Ni foam for high performances asymmetric supercapacitors. *J. Power Sources* **2016**, *312*, 156–164. [CrossRef]

73. Zhang, F.; Zhang, T.; Yang, X.; Zhang, L.; Leng, K.; Huang, Y.; Chen, Y. A high-performance supercapacitor-battery hybrid energy storage device based on graphene-enhanced electrode materials with ultrahigh energy density. *Energy Environ. Sci.* **2013**, *6*, 1623. [CrossRef]

74. Jiang, G.; Zhang, M.; Li, X.; Gao, H. $NiMoO_4$@$Ni(OH)_2$ core/shell nanorods supported on Ni foam for high-performance supercapacitors. *RSC Adv.* **2015**, *5*, 69365–69370. [CrossRef]

75. Tian, W.; Wang, X.; Zhi, C.; Zhai, T.; Liu, D.; Zhang, C.; Golberg, D.; Bando, Y. $Ni(OH)_2$ nanosheet @ Fe_2O_3 nanowire hybrid composite arrays for high-performance supercapacitor electrodes. *Nano Energy* **2013**, *2*, 754–763. [CrossRef]

76. Xu, T.; Wang, Z.; Wang, G.; Lu, L.; Liu, S.; Gao, S.; Xu, H.; Yu, Z. One-pot synthesis of a CoS-AC electrode in a redox electrolyte for high-performance supercapacitors. *J. Appl. Electrochem.* **2019**, *49*, 1069–1077. [CrossRef]

77. Cevik, E.; Bozkurt, A. Design of high-performance flexible symmetric supercapacitors energized by redox-mediated hydrogels including metal-doped acidic polyelectrolyte. *Int. J. Energy Res.* **2020**, *44*, 4309–4320. [CrossRef]

78. Baasanjav, E.; Bandyopadhyay, P.; Cho, J.S.; Jeong, S.M. Hierarchical MCo_2O_4@$Ni(OH)_2$ (M = Zn or Mn) core@shell architectures as electrode materials for asymmetric solid-state supercapacitors. *J. Energy Storage.* **2021**, *44*, 103345. [CrossRef]

79. Li, J.-J.; Hu, Y.-X.; Liu, M.-C.; Kong, L.-B.; Hu, Y.-M.; Han, W.; Luo, Y.-C.; Kang, L. Mechanical alloying synthesis of Ni_3S_2 nanoparticles as electrode material for pseudocapacitor with excellent performances. *J. Alloys Compd.* **2016**, *656*, 138–145. [CrossRef]

80. Li, R.; Wang, S.; Wang, J.; Huang, Z. Ni_3S_2@Co_S core-shell nano-triangular pyramid arrays on Ni foam for high-performance supercapacitors. *Phys. Chem. Chem. Phys.* **2015**, *17*, 16434–16442. [CrossRef]

81. Dai, C.S.; Chien, P.Y.; Lin, J.Y.; Chou, S.W.; Wu, W.K.; Li, P.H.; Wu, K.Y.; Lin, T.W. Hierarchically structured Ni_3S_2/carbon nanotube composites as high performance cathode materials for asymmetric supercapacitors. *ACS Appl. Mater. Interfaces* **2013**, *5*, 12168–12174. [CrossRef]

82. Zhao, H.; Wang, J.; Sui, Y.; Wei, F.; Qi, J.; Meng, Q.; Ren, Y.; He, Y. Construction of layered C@MnNiCo–OH/Ni_3S_2 core–shell heterostructure with enhanced electrochemical performance for asymmetric supercapacitor. *J. Mater. Sci.: Mater. Electron.* **2021**, *32*, 11145–11157. [CrossRef]

83. Long, L.; Yao, Y.; Yan, M.; Wang, H.; Zhang, G.; Kong, M.; Yang, L.; Liao, X.; Yin, G.; Huang, Z. Ni_3S_2@polypyrrole composite supported on nickel foam with improved rate capability and cycling durability for asymmetric supercapacitor device applications. *J. Mater. Sci.* **2016**, *52*, 3642–3656. [CrossRef]

84. Ye, B.; Gong, C.; Huang, M.; Ge, J.; Fan, L.; Lin, J.; Wu, J. A high-performance asymmetric supercapacitor based on Ni_3S_2-coated NiSe arrays as positive electrode. *New J. Chem.* **2019**, *43*, 2389–2399. [CrossRef]

85. Qian, H.; Wu, B.; Nie, Z.; Liu, T.; Liu, P.; He, H.; Wu, J.; Chen, Z.; Chen, S. A flexible Ni_3S_2/Ni@CC electrode for high-performance battery-like supercapacitor and efficient oxygen evolution reaction. *Chem. Eng. J.* **2021**, *420*, 127646. [CrossRef]